Velocity and anisotropy structure at the Hikurangi subduction margin, New Zealand from receiver functions

Martha K. Savage,[1,*] J. Park[2] and H. Todd[1]

[1]*Victoria University of Wellington, New Zealand. E-mail: Martha.Savage@vuw.ac.nz*
[2]*Yale University, Department of Geology and Geophysics, New Haven, CT, USA*

SUMMARY

We examine seismic velocity and anisotropy at the interface between the Australian and the subducting Pacific Plate in southern North Island, New Zealand using receiver functions from teleseismic earthquakes recorded on two L-shaped seismic arrays. IRIS station SNZO makes up the corner of the southern array. Velocity models are tested with a ray theoretical method that allows both dipping boundaries and anisotropy, assuming a 2-D structure beneath each array. The strongest arrival on the northern array consistently appears at 2 s. The arrival is modelled by a jump in velocity at a flat boundary at 12 km, which may be caused by a change in metamorphic grade. This prominent arrival correlates with a weaker arrival at 1.5 s (7 km) at station SNZO.

Isotropic layers dipping with the slab can explain many features in the first 20 s of the records, but anisotropy is needed to explain both the transverse receiver functions and a change in the polarity of a prominent *Ps* arrival at 3 s delay, relative to *P*, on the radial component. This arrival is consistent with a change between an upper layer that is either isotropic or anisotropic with a horizontal symmetry axis, and a supraslab metasediment layer having anisotropy with a vertical slow axis of symmetry. There is tradeoff between boundary dip, the plunge of the axis of symmetry, layer thickness and the amount of anisotropy. A dip of 20° (shallowing to 15° under the Tararua array), thickness of 4 km, and a vertical symmetry axis fits the backazimuth variation of the amplitudes and polarities of the arrivals with anisotropy of 4–6 per cent. Observed layer multiples are smaller than synthetic predictions. To explain this discrepancy, either layer boundaries are rough, attenuation is strong, or the layer boundaries are more gradational at the periods (1 s) used in this study compared to previous studies (∼5 s).

Key words: New Zealand, receiver functions, seismic anisotropy, seismic structure, subduction zone, synthetic seismograms, wave propagation.

1 INTRODUCTION

Plate interfaces at subduction zones, the source of the world's largest earthquakes, are critical components of the Earth system, because they are the path whereby surface materials such as water and sediments are recycled into deeper locations of the Earth's crust and mantle (Eiler 2003; Tatsumi & Kogiso 2003). As a consequence, there are concerted efforts to characterize the structure and tectonics of subduction zones using portable arrays of seismometers (Stuart *et al.* 1995; Yuan *et al.* 2000; Park & Levin 2002; Ferris *et al.* 2003) to record earthquakes and explosions. Receiver function analysis

(Langston 1977) is a popular technique that uses seismic phases converted from *P* to *S* (and sometimes *S* to *P*) at interfaces to determine the velocity contrasts. Understanding the properties of the interface may help to answer such questions as: how much water is brought into the mantle through the subduction process? What is the link between subducted sediments and seismogenesis?

Subduction zones are difficult to study with receiver functions because these plate convergence zones are thought to possess both strong anisotropy and dipping structural interfaces. Both types of features cause conversion of *P* waves to *SH*-polarized shear waves, and careful modelling is necessary to distinguish their effects. Receiver functions on stations located above subducting slabs have been used at times to constrain the dip of the slab (Park *et al.* 2002; Ferris *et al.* 2003) and the presence of sediments (Yuan *et al.* 2000). Anisotropy has been suggested in the subducting Juan de Fuca plate near Corvallis (Park *et al.* 2004), where it may be caused

*Corresponding author: Institute of Geophysics, School of Earth Sciences, Victoria University of Wellington, Box 600, Wellington, New Zealand.

by strain-aligned minerals within a detachment zone formed of serpentinite. Further north above the same plate, an attempted inversion for anisotropy was not well constrained (Frederiksen *et al.* 2003).

Combining data from the long-running broad-band permanent seismic observatory SNZO (South Karori, New Zealand), and two nearby temporary arrays, we demonstrate that the effects of both anisotropy and dipping interfaces can be observed and modelled beneath the North Island of New Zealand (NZ).

1.1 Tectonic setting

The arrays were located just north of Cook Strait on the North Island of New Zealand, which is located on the Australian plate (Fig. 1).

The arrays lie about 20 km above the subducting Pacific Plate near the southern end of the Hikurangi trench, which is a continuation of the Kermadec trench and the Lau Havre trough. Volcanism associated with backarc spreading in the western Pacific ceases approximately 200 km north of Cook Strait at Mt Ruapehu volcano. Yet intermediate-depth seismicity continues southward, until it ends abruptly about 100 km southwest of Cook Strait, coincident with the termination of the oceanic trench (Anderson & Webb 1994).

1.2 Previous work

Davey & Smith (1983) interpreted strong reflections from about 20 km depth, recorded on a refraction survey across the southern North Island, as caused by a low-velocity layer at the top of the
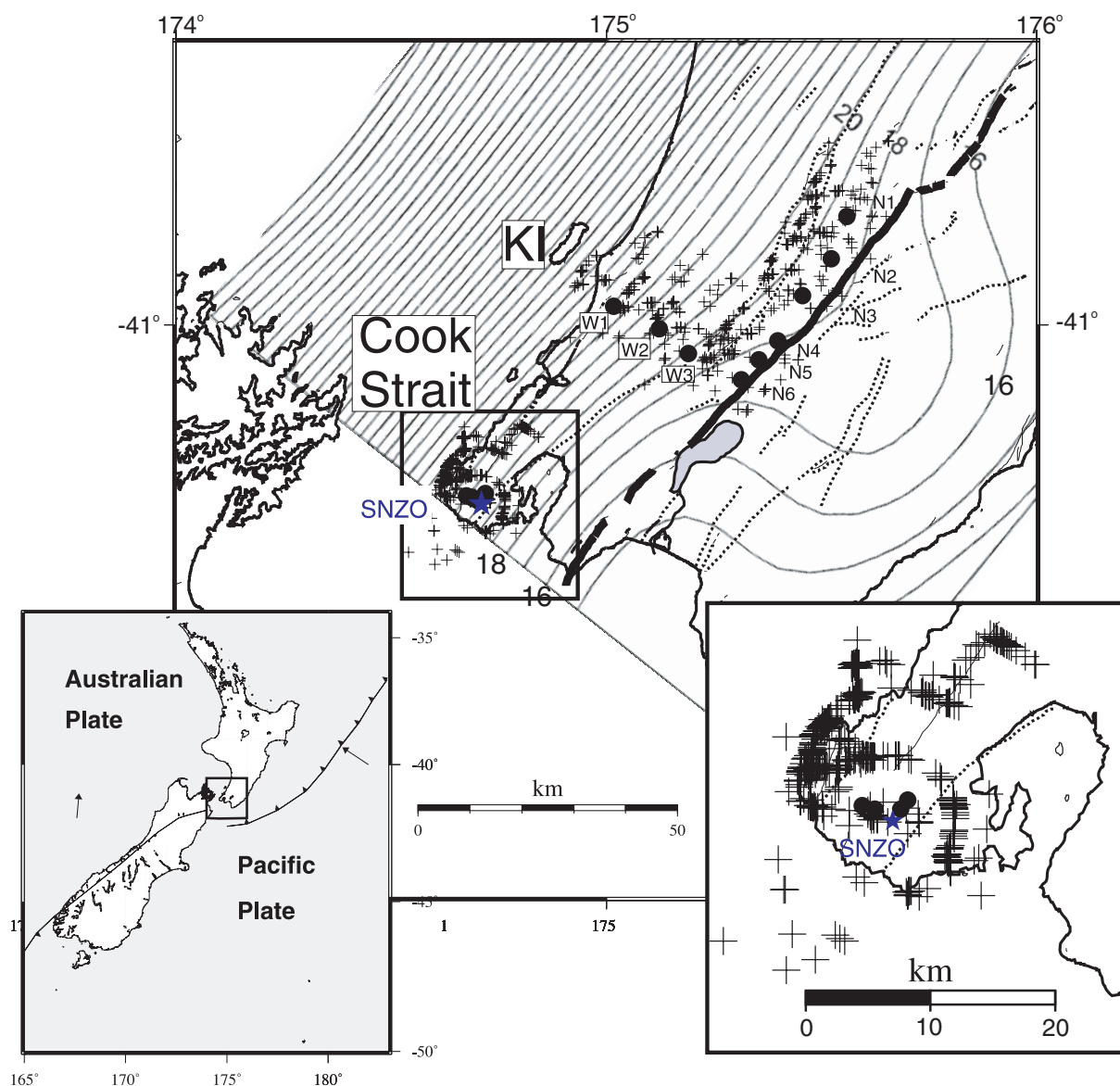

Figure 1. Tectonic setting of study area. Left inset: Australian/Pacific Plate boundary through New Zealand. Arrows represent the absolute plate motion vectors for the Australian and Pacific Plates referenced to the No Net Rotation frame, calculated based on the UNAVCO plate motion calculator in the GSRM1.2 reference frame. (Kreemer *et al.* 2003). Box is study region. Main diagram: contours of the plate interface in intervals of 1 km are from (Reading *et al.* 2001). KI: Kapiti Island. The arrays are shown as circles, with permanent station SNZO as the labelled star. Tararua stations are labelled W1-W3 and N1-N6. Karori–Makara array stations plot on top of each other and are not labelled. Coast, lakes and rivers are solid lines. Faults are dashed, except the Wairarapa fault, which is in bold. Crosses are 'piercing points' where the surface projection of the *P-S* conversions would occur in the AK135 model (Kennett *et al.* 1995) for a depth of 35 km. Box is region expanded in the right inset.

plate interface, dipping at 15° to the northwest. Robinson (1986) inverted earthquake traveltimes at the Wellington regional seismic network to determine a velocity model with dipping isotropic layers to 60 km depth. Eberhart-Phillips & Reyners (1997) found similar but more complicated features in a 3-D traveltime inversion for velocity in the region. Reading *et al.* (2001) inverted direct *P*, *S*, and converted *SP* and *PS* phases from local earthquakes for shallow *P* wave velocity structure and the depth to the slab interface. This last study included the stations used in this paper. Brisbourne & Stuart (1998) determined shear wave velocities to 150 km depth from surface waves, again using some of the stations discussed in this paper. These same data were later inverted for anisotropy structure, in combination with shear wave splitting data (Brisbourne *et al.* 1999).

This study addresses the nature of the top of the slab. Savage (1998) interpreted receiver functions recorded at station SNZO as showing phases converted from an approximately 7.5-km-thick anisotropic layer extending from 28 to 35.5 km depth, at the location of the metamorphosed subducting crust and the top of the slab. Bourne & Stuart (2000) interpreted precursors to *ScS* waves as conversions to *P* waves from the base of the subducting Pacific crust, and from the top of the subducting plate. They also modelled the thickness of the subducting crust in the Tararua region as 11–14 km thick. A 1–2 km thick sediment layer was postulated to lie at the top of the subducting plate to explain the remaining *ScSp* waveform. However, Reading *et al.* (2001) saw no phases corresponding to the expected low-velocity zone, using converted phases from local earthquakes recorded on the Tararua stations. From the depth separation of a double seismic zone, they considered that the subducted oceanic crust under the southern North Island was 16 ± 2 km, thickened compared to normal oceanic lithosphere (typically 7–8 km). Receiver functions using phases converted from teleseisms recorded on the Tararua array have been examined in a doctoral thesis and an Honours thesis (Shafkit 1997; Todd 2002). Studies in other regions of New Zealand have also suggested a low velocity at the top of the plate (Bannister 1988; Luo 1992; Reading 1996; Chadwick 1997; Eberhart-Phillips & Reyners 1999; Reading *et al.* 2001; Louie *et al.* 2002), which has been interpreted as a thin sediment layer. Magnetotelluric sounding (Ingham *et al.* 2001) also suggested that a layer of thin (2.5 km thick), highly conductive (5–10 ohm-m) sediments lay at the top of the plate interface in the eastern North Island, at a depth of about 12–14 km.

In contrast, Gubbins & Snieder (1991) modelled the dispersion of *P* waves from events in the Tonga-Kermadec deep seismic zone recorded at a station in Wellington and suggested a high velocity eclogite layer of thickness between 6 and 15 km close to the top of the slab. A surface wave study (Brisbourne & Stuart 1998) also suggested that high velocities observed with *Pn* data (Chadwick 1997; Galea 1992) could not be thicker than about 10 km.

This study aims to examine these discrepancies in the southern North Island and to investigate the interplay between anisotropy and dipping boundaries in the receiver functions, and also to determine if scattering from isotropic structure could have caused the previously reported energy on transverse receiver functions at SNZO, which was interpreted as anisotropy (Savage 1998). Such clarification helps determine the nature of the rocks and thickness of the sediments and oceanic crust entering the subduction zone.

2 DATA

We use seismograms from two temporary broad-band arrays and permanent IRIS station SNZO (Fig. 1). Most of the earthquakes
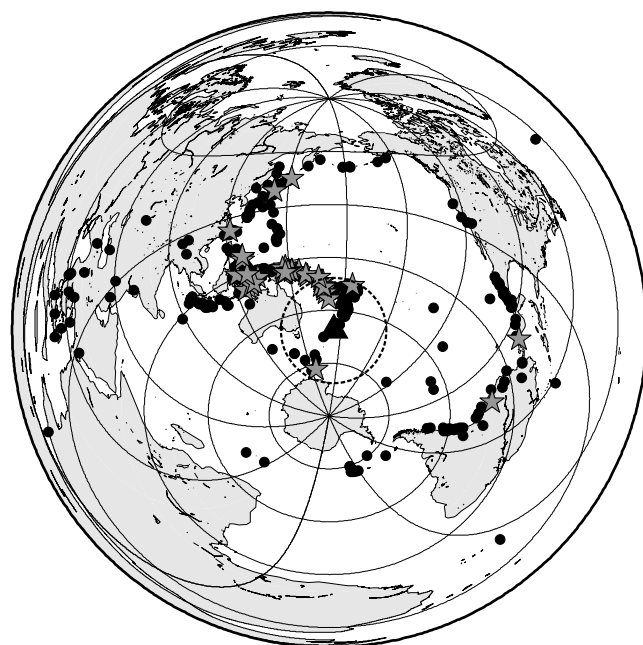

Figure 2. Distribution of data used. Circles are events recorded at station SNZO (triangle). The stars are events recorded at the Tararua array. The dashed circle delineates a radius of 30° around SNZO, from which events are excluded in Figs 4–8.

arrive from the South Pacific subduction zones, to the northwest of the array (Fig. 2). We include global earthquakes with $M > 6.3$, plus events with $5.4 < M < 6.3$ at epicentral distances $30° < \Delta < 60°$. *P* phases are typically used for epicentral distances Δ out to 110°, and *PKP* beyond 110° (Fig. 2). Close events are used to examine moveout with distance, but only events with $\Delta > 30°$ are used in the comparisons with synthetics. The piercing points of phases converted from *P* to *S* at the Moho are nearly directly underneath the stations (Fig. 1).

The northern Tararua array was located in the Tararua Ranges from 1991 January–1992 September (Stuart *et al.* 1995). The array consisted of two arms: a 37-km, six-station arm running northeastwards, and a 27-km, four-station arm (including a common station), orthogonal to the first (Fig. 1). The nine instruments ranged in elevation between 130 and 280 m. They were located on Mesozoic greywacke and used three-component broad-band Guralp CMG-3T seismometers with RefTek digital recording equipment. 452 phases from 105 earthquakes were used, of which 13 were *PKP* phases from five earthquakes with $113° < \Delta < 147°$. From the locations of the pierce points for *P–S* conversions beneath the stations compared to the depth to the top of the slab reported in Reading *et al.* (2001), we calculate a change from 17 to 28 km depth to the slab interface over a distance of 43.3 km, or a dip of 14° (Fig. 1).

The southern, Karori–Makara array, consisted of four portable stations aligned northeast and northwest of permanent station SNZO to form a five-station L-shaped array in the Wellington region, with station spacing of 1–1.5 km. Guralp CMG40T broad-band seismometers recorded on Orion digital recording equipment from January through December, 1998 (Stewart 1998). SNZO is a permanent broad-band observatory that has been maintained by IRIS since 1992. We include phases from SNZO recorded through the year 2003 for a total of eleven years of data (Table 1 and Fig. 2). From the locations of the pierce points for *P–S* conversions, we calculate

Table 1. Station locations for the Karori–Makara and SNZO stations. # denotes number of events used from that station.

STA	Latitude (°)	Longitude (°)	Elevation (m)	#
EGB2	−41.3017	174.6754	376	11
SEF2	−41.3034	174.6880	89	14
RKK2	−41.3036	174.7126	134	8
SAL2	−41.2961	174.7195	237	7
SNZO	−41.31030	174.7046	62	443

a change from 19–25 km depth to the slab interface over a distance of 16.7 km, or a dip of 20° (Fig. 1).

3 METHODS

Receiver functions (RFs) infer *P*-to-*S* conversions of teleseismic waves to determine the nature of boundaries in earth structure (Langston 1977; Owens *et al.* 1984). To compute an RF, we deconvolve the vertical component from the radial and transverse components to separate a structure 'response' from the source and instrument responses. The deconvolved radial and transverse components are called the receiver functions. The transverse receiver function is zero in an isotropic, horizontally layered earth. Dipping isotropic layers or anisotropy can cause large transverse energy and variations with earthquake-station backazimuth (Cassidy 1992; Levin & Park 1997, 1998; Savage 1998).

We determine receiver functions using multitaper correlation estimates of the first 20 s of the data (Park & Levin 2000). This method computes receiver functions in the frequency domain, avoiding numerical instabilities associated with using spectral division. It also distinguishes between coherent and incoherent energy to remove noise, and weights receiver functions based on their noise level. It has been particularly useful in the noisy environment in New Zealand.

Several frequency bands were examined. High frequencies provide coherent energy across most backazimuths at a given station, but are not as well correlated across stations. Therefore, to simplify analysis and concentrate on the main structures, we present results for cutoff frequency 1 Hz. (A cosine-squared taper from 0.5 to 1.0 Hz multiplies the RF in the frequency domain to suppress bandedge effects.)

At each station, we form composite receiver functions in bins of 5° spacing and with overlap of 10° by stacking the RFs from single events. Individual seismic records therefore contribute to the composite receiver functions in two adjacent bins. The individual receiver functions are weighted by their inverse variance (i.e. noisy records have higher variance and so are weighted less strongly), which makes a careful analyst assessment of RF quality less necessary.

Because the focus of this paper is on the shallow structure, moveout corrections are less than 0.36 s for the Moho phase, and were not applied.

We model the seismograms using a ray-theoretical method that allows inclusion of both anisotropy and dipping boundaries (Frederiksen & Bostock 2000). This method models the first few multiples well, when simple models with few layers are used. We use an incident plane *P* wave as our source, using the exact station–earthquake geometry of the data. We analyse the synthetic waveforms with the same receiver function codes, and using the same distribution and stacking bins as the data set, in order to calculate waveforms that will most closely resemble the data. In particular, *P*s moveout will affect the synthetic data set in the same way as the

data. For simplicity, most of the models consider anisotropy axes to be horizontal or vertical.

4 RESULTS AND INITIAL INTERPRETATION

To see whether dipping layers or anisotropy affect the data, we compare computed RFs as a function of backazimuth (Fig. 3). Dipping isotropic layers are expected to yield the strongest initial radial peaks for the direct *P* phase travelling downdip (backazimuth 145°) and weakest for waves arriving updip (backazimuth 315°), due to perturbations in the angle of incidence. Transverse arrivals should be weak for backazimuth updip or downdip of the slab, and should change polarities about the slab dip direction (Cassidy 1992). It is not possible to get a good comparison of all backazimuths for the portable arrays, which operated for a shorter interval than SNZO. The major features have been labelled 1–4.

4.1 Radial receiver functions

The strength of the direct arrival (labelled 1 in Figs 3 and 4) varies markedly with backazimuth, caused by the dip of the slab, and also the changes in angles of incidence (i.e. closer epicentral distance) for the earthquakes in different backazimuth ranges (Fig. 2).

The arrival labelled 2 appears as a 'knee' to the SNZO station direct arrival from 270°–360°, and comes in at 1.5 s after the direct arrival. We interpret it as interference due to multiple arrivals from shallow layers with the conversion from a midcrustal boundary (Savage 1998). The 'knee' is either absent or comes in earlier at 80°–180°. For the Tararua array, arrival 2 is somewhat later (2 s after direct *P*). The trough labelled '3', which arrives at 3–4 s on SNZO, is stronger on SNZO than at the Tararua array stations at these backazimuths. Finally, the arrival labelled 4 at 5 s after the initial *P* on both sets of stations was previously interpreted as the Moho (the base of the oceanic crust, within the slab) (Savage 1998; Bourne & Stuart 2000). The Karori–Makara station RFs are close to the SNZO results, suggesting that the *Ps* converted phases we identify are not caused by local structure or topography near SNZO.

Strikingly, and most evident at SNZO with its broader azimuthal range, the radial arrivals change polarity, so that the radial *P*s pulses at backazimuth 60°–180° are almost opposite in phase for arrivals 2, 3, and 4 compared to 280°–360° backazimuth. Such opposition in phase is common for transverse components in the case of both dipping boundaries and anisotropic material, but occurs for radial components less commonly, and suggests anisotropy that affects the *P*s converted wave more strongly than the isotropic velocity jump (e.g. Park *et al.* 2004), or that strong dips are present (see below, Section 4.3).

Radial RFs for the Tararua western and northern arms are similar but differ in small ways (Figs 3, 5 and 6). The western arm has a later initial peak (1), probably caused by its proximity to sediment-filled valleys relative to the northern arm, which is located higher in the mountains. The later peak in the western arm results in the northern arm having a stronger and earlier trough after its initial peak, but phase (2) arrives at the same time (2 s) on both arms of the array. The northern arm has a fairly strong trough-peak combination from 3–5 s (arrivals 3 at 3 s and 4 at 4 s). On the western arm, the trough (3) arrives at the same time (3s) but is weaker than the northern arm trough, and the peak (4) arrives later (4.5–5 s) and is also weaker (most evident in Fig. 5).
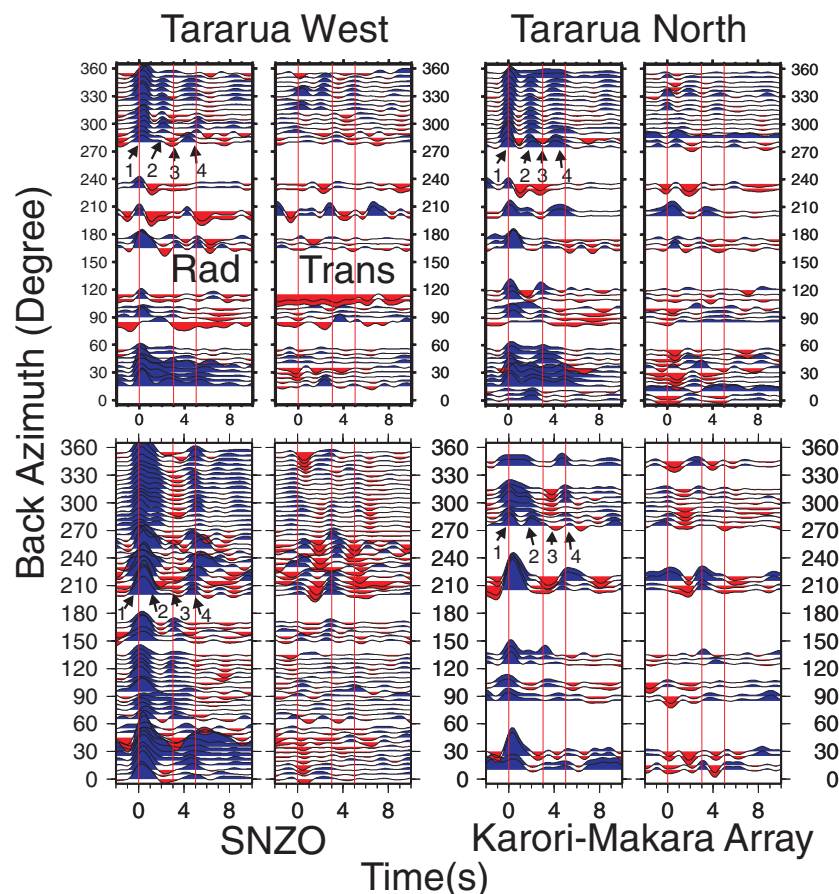
Figure 3. Receiver functions plotted as a function of backazimuth. Earthquakes of all epicentral distances are included. Within each set of plots, the left-hand plot contains the radial components, while the right-hand plot contains the transverse components. The top two sets of plots are stacked receiver functions for the Tararua array, labelled West for stations W1–W3 (Fig. 1) and North for stations N1–N6. Bottom left is for station SNZO, and bottom right is the stacked set of arrivals from the Karori–Makara array. Note the change in convention for the polarity of the transverse component between this paper and those plotted in (Savage 1998). The radial and transverse plots have the same scale. Lines are plotted at 0, 3 and 5 s to facilitate comparisons. Labelled arrows denote phases discussed in the text.

Arrival 2, which we call the 'mid-crustal positive' at 2 s is apparent on all the stations, and increases in amplitude relative to the initial arrival both from northeast to southwest (i.e. the stations located in the Tararua ranges) and from northwest to southeast (Figs 5–6). This trend is apparent in both the backazimuthal ranges of 315°–360° and 270°–315°, which straddle the downdip direction of the slab. In contrast to the amplitude variation, the arrival time of the mid-crustal positive arrival is stable at 2 s across both sections.

4.1.1 Interpretation of phase (2)

This consistent 2 s time delay suggests scant dip in the layer across the array (Figs 3–6). Simple isotropic forward modelling with three layers, with 4.6 km s^{-1} for the P wave in the upper layer, leads to 11.8 km depth to the first interface under the Tararua array. However, the corresponding arrival (2) at SNZO is about 0.5 s earlier than that at the Tararua array, suggesting that the converting boundary is shallower under SNZO. Using a rough scaling of 8 km s^{-1} of S–P time, the interface should be 4 km shallower under SNZO than that under the Tararuas, fitting with 6.7 km to the depth of the layer determined by Garrick (1968). Inverse modelling using linearized inversions of receiver functions, both simple (Ammon *et al.* 1990)

and with the addition of constraints (Özalaybey *et al.* 1997) based on the surface wave results of (Brisbourne & Stuart 1998), required low velocities near the surface to reproduce the large amplitudes for the mid-crustal positive arrival.

The lack of change in Ps delay time suggests that the amplitude change of arrival (2) is caused by changing velocity of the lower layer, that is, it must be getting larger from north to south and from west to east. The velocity change seems likely to be caused by the transition from velocities reported by (Reading *et al.* 2001) in their layers 2 and 3, which occurs at about 12 km. While the velocity variation in their layer 2 is indeed minimal, varying only between 5.6 and 5.8 km s^{-1} across the array, the velocity in layer 3 does not vary in their inversion as we would expect from the above analysis.

We interpret the jump in velocity that causes the mid-crustal positive Ps conversion to be caused by a change from consolidated greywacke of the Torlesse group that outcrop at the surface, to the 'metamorphic' layer suggested by Garrick (1968). This layer could either be another type of more consolidated greywacke, metamorphosed greywackes or schists. Such a large change in velocity is unusual in NZ (T. Stern, private communication), but may be caused by the change from the greywackes of the early Mesozoic Torlesse Rakaia terrane to the schistose Waipapa Terrane (Mortimer *et al.* 1997) at depth. A similar sharp gradient in velocity is also seen
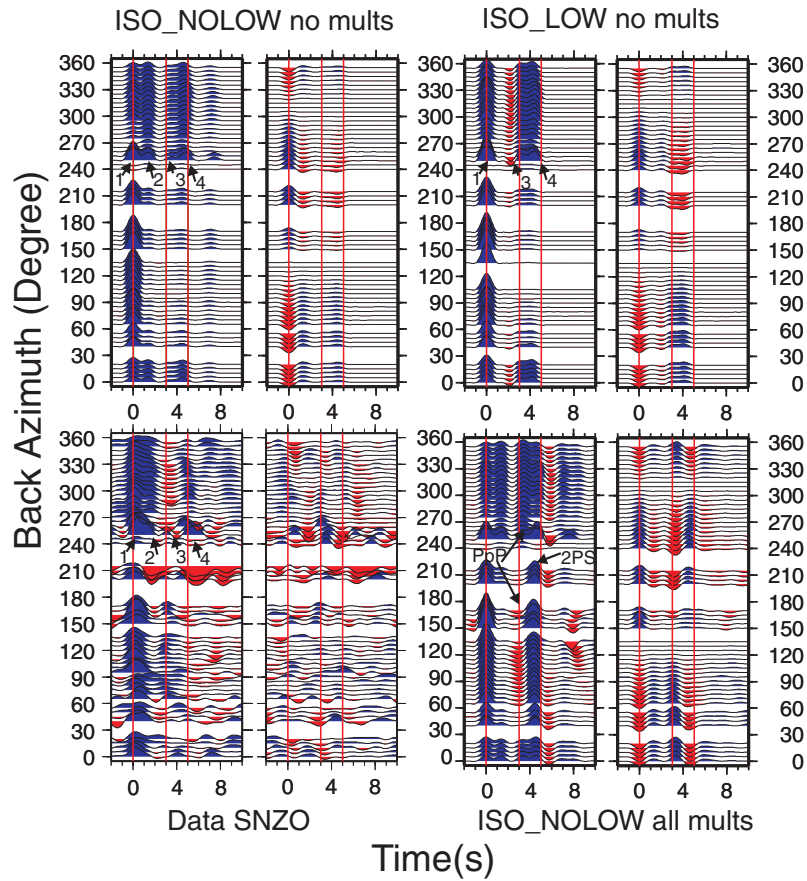
Figure 4. Comparison of receiver functions for epicentral distances greater than 30°, plotted as in Fig. 3, for SNZO data (bottom left-hand panel), with models for isotropic dipping layers. Top left-hand panel: model ISO_NOLOW (Table 2) calculated with only direct converted phases. Bottom right-hand panel: model ISO_NOLOW calculated with all multiple reflections and conversions. Top right-hand panel: model ISO_LOW (Table 2) with only direct conversions.
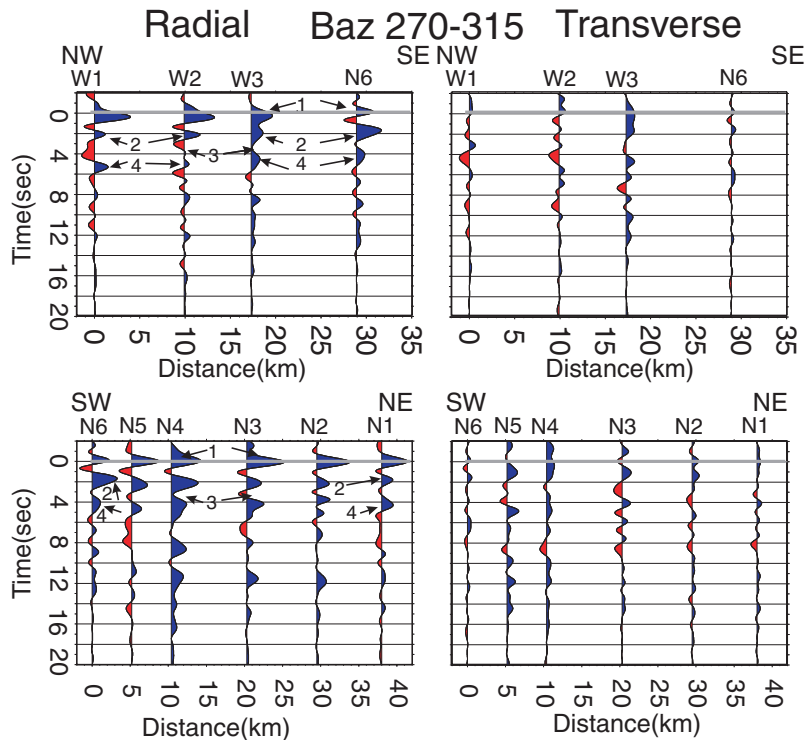

Figure 5. Receiver functions, processed as in Fig. 3, and then stacked over the backazimuth range 270°–315°, at individual Tararua array stations. The top two plots are for the southern, short arm of the array and the bottom two plots are for the northern, long arm of the array. Distance is measured from the station at the left of the plot.
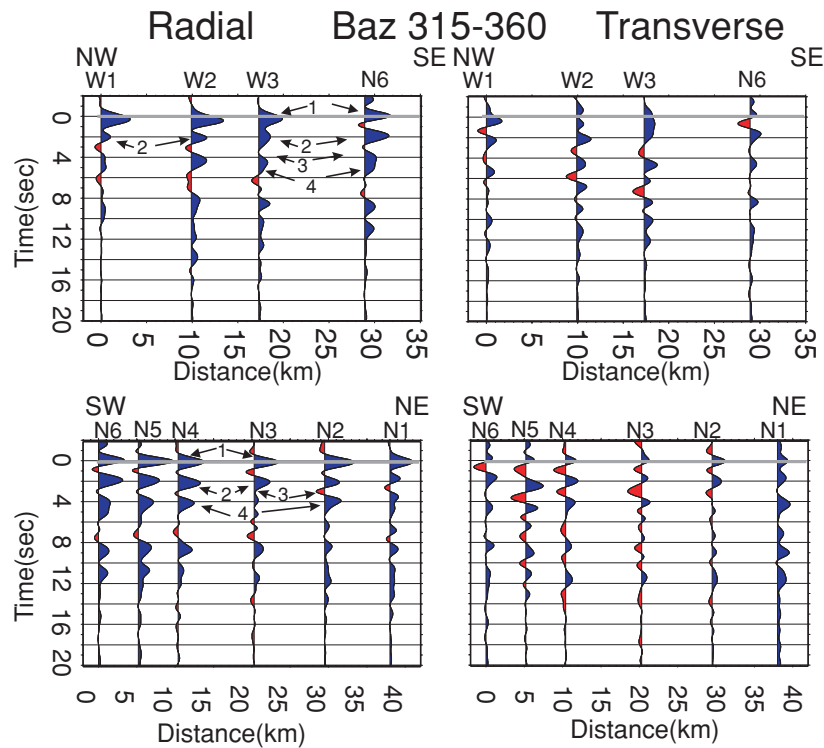
Figure 6. Same as Fig. 5, but for the backazimuth range 315°–360°.

at about this depth in the tomographic modelling just south of the Tararua array (Eberhart-Phillips & Reyners 1997). If the lower crust contains schists, then they are not lying flat, as in that case their symmetry axis would be vertical, and we show below that arrival (3) is fit best if the lower crust is isotropic or has a near-horizontal symmetry axis. Lower crustal anisotropy with a horizontal symmetry axis was also suggested from receiver functions recorded on the nearby northern South Island (Wilson *et al.* 2004). Shearing of these rocks parallel to the plate boundary during the present oblique compression and also during the past strike-slip deformation (Walcott 1987) is a likely cause of the anisotropy.

4.1.2 Interpretation of phases (3) and (4)

The later arrivals are consistent with the association of phase (4) with the subducting oceanic crust, since it would be shallower under the northern arm than under the western arm (Figs 1, 3, 5 and 6). At stations in the north arm, which are at about 29 km from the westernmost station, the phase arrives at about 4.0 s, compared to 5.0 s at station W1. This trend is most apparent for radial arrivals from 270° to 315° (compare Fig. 5 with Fig. 6). Using the rough scaling of 8 km s^{-1} between the *S-P* times, we calculate a dip of 15°, similar to the 14° dip calculated in Section 2. The amplitude of the phase (4) at 4–5 s is typically less than phase (2), and its amplitude varies irregularly across the array. The true dip could be somewhat larger than the apparent dip of 15° determined above, because of the changing velocity beneath layer 2 as suggested above by the amplitude change in phase (2).

The trough labelled '3' in Fig. 3 is interpreted as caused by a low-velocity layer at the top of the slab (see below). It is either absent or smaller in the Tararua array stations than at SNZO, and it arrives at a somewhat earlier time at the Tararua stations. The smaller amplitude could be caused by a thinner layer of sediments,

the shallower slab dip in the region, or a smaller velocity contrast between the sediments and the midcrust.

4.2 Transverse receiver functions

The transverse RFs for the Karori–Makara portables agree with SNZO for the ranges 270°–300° and 210°–240° where they are best represented (Fig. 3). However, the transverse arrivals differ more between the other data sets. For the Northern arm, they change coherently across the array for ranges 315°–360° (Fig. 6). However, for the other stations and for other backazimuths on these stations, the energy is not as coherent and the resultant stacks are therefore small (Fig. 3). The energy on the transverse arrivals at the initial *P* arrival from station SNZO is offset in phase to that from the Tararua stations.

One of the striking features at SNZO is the strong energy on the transverse components from backazimuth 180° to 270° (Fig. 3). This is accompanied by radial arrivals that are strong for the Moho arrival (4), but less coherent between (1) and (4). The effect is weaker when events from distance less than 30° are excluded (Fig. 4).

4.3 Synthetic seismograms

Station SNZO has much better backazimuth coverage than the two portable arrays, so we concentrate first on matching the RFs at SNZO. We do not specifically include the Karori–Makara stations in this comparison, because they mainly confirm the arrivals at SNZO (Fig. 3). We begin by examining isotropic models and then consider anisotropy.

4.3.1 Isotropic models: fit to SNZO

Model ISO_NOLOW uses five layers to approximate the 9-layer dipping model sn5 examined in Savage (1998) (Table 2). It is isotropic,

Table 2. Velocity models discussed in text. Mod is model name. Th is layer thickness. ρ is density. Iso is a code given as 1 if isotropic and 0 if anisotropic. Per cent P is P-wave anisotropy, per cent S is S-wave anisotropy, with negative numbers denoting a slow axis of symmetry. Tr is the azimuth of the axis of symmetry measured from N, Pl is the plunge of the axis of symmetry, measured from horizontal in the Tr direction. St is the strike of the top of the interface. Dip is the dip of the top of the interface, measured from horizontal according to the right-hand rule in the convention of (Aki & Richards 1980). Dep is the depth to the bottom of the interface.

Model/layer no.	Th (m)	ρ (kg m^{-3})	Vp (ms^{-1})	Vs (ms^{-1})	Iso	Per cent P	Per cent S	Tr (°)	Pl (°)	St (°)	Dip (°)	Dep (m)
ISO_NOLOW/1	8200	2227	4577	2615	1	0	0	0	0	0	0	8200
ISO_NOLOW/2	16 800	2750	6097	3484	1	0	0	0	0	221	15	25 000
ISO_NOLOW/3	10 000	2930	6750	3860	1	0	0	0	0	221	15	35 000
ISO_NOLOW/4	25 000	3336	8026	4586	1	0	0	0	0	221	15	60 000
ISO_NOLOW/5	0	3550	8680	4960	1	0	0	0	0	0	0	
ISO_LOW/1	20 000	2690	6000	3429	1	0	0	0	0	0	0	20 000
ISO_LOW/2	2000	2402	5100	2550	1	0	0	0	0	225	20	22 000
ISO_LOW/3	11 000	2882	6600	3771	1	0	0	0	0	225	20	33 000
ISO_LOW/4	50 000	3362	8100	4629	1	0	0	0	0	225	20	85 000
ISO_LOW/5	0	3362	8100	4629	1	0	0	0	0	0	0	
ANID20/1	6700	2307	4694	2640	1	0	0	0	0	0	0	6700
ANID20/2	21 300	2690	6030	3450	0	−4	−4	135	0	220	20	28 000
ANID20/3	4000	2402	5100	2550	0	−4	−4	135	90	220	20	32 000
ANID20/4	8000	2930	6750	3860	0	−6	−6	135	0	220	20	40 000
ANID20/5	80 000	3370	8140	4570	0	7	5	62	0	220	20	120 000
ANID20/6	0	3370	8140	4570	1	0	0	0	0	0	0	
ANI2FLATD20/1	6700	2307	4694	2640	1	0	0	0	0	0	0	6700
ANI2FLATD20/2	21 300	2690	6030	3450	0	−4	−4	135	0	0	0	28 000
ANI2FLATD20/3	4000	2402	5100	2550	0	−4	−4	135	90	220	20	32 000
ANI2FLATD20/4	8000	2930	6750	3860	0	−6	−6	135	0	220	20	40 000
ANI2FLATD20/5	80 000	3370	8140	4570	0	7	5	62	0	220	20	120 000
ANI2FLATD20/6	0	3370	8140	4570	1	0	0	0	0	0	0	
ANID15/1	6700	2307	4694	2640	1	0	0	0	0	0	0	6700
ANID15/2	21 300	2690	6030	3450	0	−4	−4	135	0	220	15	28 000
ANID15/3	4000	2402	5100	2550	0	−4	−4	135	90	220	15	32 000
ANID15/4	8000	2930	6750	3860	0	−6	−6	135	0	220	15	40 000
ANID15/5	80 000	3370	8140	4570	0	7	5	62	0	220	15	120 000
ANID15/6	0	3370	8140	4570	1	0	0	0	0	0	0	
ANI2ANID15/1	10	2307	4694	2640	1	0	0	0	0	0	0	10
ANI2ANID15/2	6690	2307	4694	2640	0	−4	−6	45	0	0	0	6700
ANI2ANID15/3	21 300	2690	6030	3450	0	−4	−4	135	0	220	15	28 000
ANI2ANID15/4	4000	2402	5100	2550	0	−4	−4	135	90	220	15	32 000
ANI2ANID15/5	8000	2930	6750	3860	0	−6	−6	135	0	220	15	40 000
ANI2ANID15/6	80 000	3370	8140	4570	0	7	5	62	0	220	15	120 000
ANI2ANID15/7	0	3370	8140	4570	1	0	0	0	0	0	0	
ANI2ANIP5D15/1	10	2307	4694	2640	1	0	0	0	0	0	0	10
ANI2ANIP5D15/2	6690	2307	4694	2640	0	−4	−6	45	0	0	0	6700
ANI2ANIP5D15/3	21 300	2690	6030	3450	0	−4	−4	135	5	220	15	28 000
ANI2ANIP5D15/4	4000	2402	5100	2550	0	−4	−4	135	95	220	15	32 000
ANI2ANIP5D15/5	8000	2930	6750	3860	0	−6	−6	135	5	220	15	40 000
ANI2ANIP5D15/6	80 000	3370	8140	4570	0	7	5	62	5	220	15	120 000
ANI2ANIP5D15/7	0	3370	8140	4570	1	0	0	0	0	0	0	
ANI2ANIP90D20/1	10	2307	4694	2640	1	0	0	0	0	0	0	10
ANI2ANIP90D20/2	6690	2307	4694	2640	0	−4	−6	45	0	0	0	6700
ANI2ANIP90D20/3	21 300	2690	6030	3450	0	−4	−4	135	90	220	20	28 000
ANI2ANIP90D20/4	4000	2402	5100	2550	0	−4	−4	135	90	220	20	32 000
ANI2ANIP90D20/5	8000	2930	6750	3860	0	−6	−6	135	0	220	20	40 000
ANI2ANIP90D20/6	80 000	3370	8140	4570	0	7	5	62	0	220	20	120 000
ANI2ANIP90D20/7	0	3370	8140	4570	1	0	0	0	0	0	0	
ANI2ANI3ISOD20/1	10	2307	4694	2640	1	0	0	0	0	0	0	10
ANI2ANI3ISOD20/2	6690	2307	4694	2640	0	−4	−6	45	0	0	0	6700
ANI2ANI3ISOD20/3	21 300	2690	6030	3450	1	0	0	0	0	220	20	28 000
ANI2ANI3ISOD20/4	4000	2402	5100	2550	0	−4	−4	135	90	220	20	32 000
ANI2ANI3ISOD20/5	8000	2930	6750	3860	0	−6	−6	135	0	220	20	40 000
ANI2ANI3ISOD20/6	80 000	3370	8140	4570	0	7	5	62	0	220	20	120 000
ANI2ANI3ISOD20/7	0	3370	8140	4570	1	0	0	0	0	0	0	
ANI_OC14D20/1	6700	2307	4694	2640	1	0	0	0	0	0	0	6700
ANI_OC14D20/2	14 300	2690	6030	3450	0	−4	−4	135	0	220	20	21 000
ANI_OC14D20/3	4000	2402	5100	2550	0	−4	−4	135	90	220	20	25 000
ANI_OC14D20/4	10 000	2930	6750	3860	0	−6	−6	135	0	220	20	35 000

Table 2. (*Continued*.)

Model/layer no.	Th (m)	ρ (kg m^{-3})	Vp (ms^{-1})	Vs (ms^{-1})	Iso	Per cent P	Per cent S	Tr (°)	Pl (°)	St (°)	Dip (°)	Dep (m)
ANI_OC14D20/5	80 000	3370	8140	4570	0	7	5	62	0	220	20	120 000
ANI_OC14D20/6	0	3370	8140	4570	1	0	0	0	0	0	0	
ANIOC11D20/1	6700	2307	4694	2640	1	0	0	0	0	0	0	6700
ANIOC11D20/2	19 300	2690	6030	3450	0	−4	−4	135	0	220	20	26 000
ANIOC11D20/3	4000	2402	5100	2550	0	−4	−4	135	90	220	20	30 000
ANIOC11D20/4	7000	2930	6750	3860	0	−6	−6	135	0	220	20	37 000
ANIOC11D20/5	80 000	3370	8140	4570	0	7	5	62	0	220	20	120 000
ANIOC11D20/6	0	3370	8140	4570	1	0	0	0	0	0	0	
TAR/1	12 000	2307	4694	2640	1	0	0	0	0	0	0	12 000
TAR/2	12 000	2690	6030	3450	0	−4	−4	135	0	0	0	24 000
TAR/3	4000	2402	5100	2550	0	−4	−4	135	90	220	12.6	29 000
TAR/4	10 000	2930	6750	3860	0	−6	−6	135	0	220	12.6	39 000
TAR/5	80 000	3370	8140	4570	0	7	5	62	0	220	12.6	119 000
TAR/6	0	3370	8140	4570	1	0	0	0	0	0	0	

with no low-velocity layers, and has interfaces dipping 15° to the northwest at 8.2, 25, 35 and 60 km directly beneath SNZO. The dip and the strong velocity contrast at 8.2 km cause the radial RF peak associated with this interface to be larger than the radial RF at zero time delay for 250°–350° backazimuth (Fig. 4). The more gradational velocity contrasts in model sn5 (Savage 1998) produced larger initial radial pulses, which were closer to the data. For isotropic dipping models, there is symmetry about the dip axis; the transverse *P*s converted phases change polarity about the updip and downdip directions, and the radial components are symmetric about these directions (Cassidy 1992). The synthetic composite RFs are not symmetric, however, due to the uneven earthquake distribution and associated moveout effects (Fig. 2).

Many of the features of the real data are seen in the synthetics without the multiples (Fig. 4). The initial radial RF pulse is wider in the data between backazimuth 180°–360° than 60°–180°. The synthetics are similar in that the 1.5-s arrival is near-absent from backazimuth 60° to 180°. The positive arrival (4) at about 5 s in the synthetic RFs from the Moho is lacking for 60°–180° backazimuth for both the observations and the multiple-free model computation. This is because, for these backazimuth, earthquakes are either closer than 30° (and so not included in the azimuthal stacks) or more distant than 90° (Fig. 2). The near vertical incidence of these distant events causes little energy to be converted to *S* waves, hence the majority of the energy is in the direct *P* arrival. Other common features for composite RFs computed from the data and for isotropic model ISO_NOLOW, particularly without multiples, include the generally larger amplitudes on the transverse arrivals from backazimuth 200° to 270°, the general pattern of polarity change of the transverse arrivals between 180° and 360° and the generally weaker arrivals on the initial radial *P* wave around 60° and 270°.

Including the multiples yields a worse fit to the data. There is a strong pair of arrivals on the synthetics between 3 and 5 s and fairly strong energy out to 9 s, which is caused by the multiples from the top layer (Fig. 4). The first arriving multiple, *PpP*, arrives at 3 s with negative polarity on the radial component from backazimuth 60° to 180° and positive polarity between backazimuth 250° and 360°. This change in polarity occurs because of the layer dip (Fig. 7), a phenomenon also described by Lucente *et al.* (2005). Flat-layer models have *PpP* arriving with a negative polarity if the layer increases in velocity with increasing depth, due to the reversal of polarity at the surface but not at the layer interface. When *PpP* arrives from the updip direction, that is, 60°–180° in our case, the same principle ap-

plies. But when *PpP* arrives from the downdip direction, 240°–360°, the geometry causes the surface reverberation to arrive at an angle greater than 90° to the interface. This in turn causes the phase to arrive from the anti-radial direction, in effect reversing its polarity a second time, so that *PpP* has positive polarity at the surface. Note also that with dipping layers, the free-surface incidence angle of the multiples differs from that of the direct arrival.

RFs for SNZO data have a reversal in polarity with backazimuth at a similar time as the above synthetics, but with the opposite polarity. It is tempting to try to modify this model to match these polarities. However, when we change the surface layer to high velocity, the multiples have the right polarity, but the direct *Ps* phase has opposite polarity to what we observe. When we reverse the layer dip, we again match the polarities at 3 s, but the strong initial *Ps* phases appear at 60°–180° backazimuth, in contrast to the observed RFs. Multiple arrivals tend to be larger in synthetics than in real data, much more than one would expect from simple attenuation (e.g. Park & Levin 2006). These differences may be caused by greater scatter in the multiples due to the lack of sharp planar boundaries. This appears to be true for the multiple arrival at 4.5 s, which is absent in the data and also in the synthetics made without multiples, for backazimuths 60°–180°. Thus, we consider that direct *Ps* from a feature such as a low-velocity layer should be considered to explain the negative arrival at 3 s for backazimuth 240°–360°. This is supported by the trough (3) arriving at the same time at the Tararua array (Figs 3, 5 and 6) despite later appearance of arrival (2), whose multiple should therefore be later still. Finally, a low-velocity layer was interpreted at the top of the slab on the basis of *ScSP* precursors (Bourne & Stuart 2000).

We next consider a model based on that of Bourne & Stuart (2000), derived for station SNZO (Table 2; Fig. 4). Our model ISO_LOW adds a 20° dip to the layers in the isotropic (Bourne & Stuart 2000) model, whose major feature is a 2-km-thick low-velocity layer at the top of the slab. This low-velocity layer produces a negative arrival at about 2.5 s, which is closer to the data than the model ISO_NOLOW. However, the positive polarity for the 3-s arrival from 60° to 180° does not appear in either isotropic model. The two conversions from the Moho and the top of the slab in model ISO_LOW form a broad positive pulse between 3 and 5 s. These arrivals are both stronger and broader than the corresponding arrivals in the data, suggesting either weaker velocity contrasts or more gradational boundaries in the subsurface rock. In addition, the set of negative-to-positive arrivals in the model come in about 0.5 s
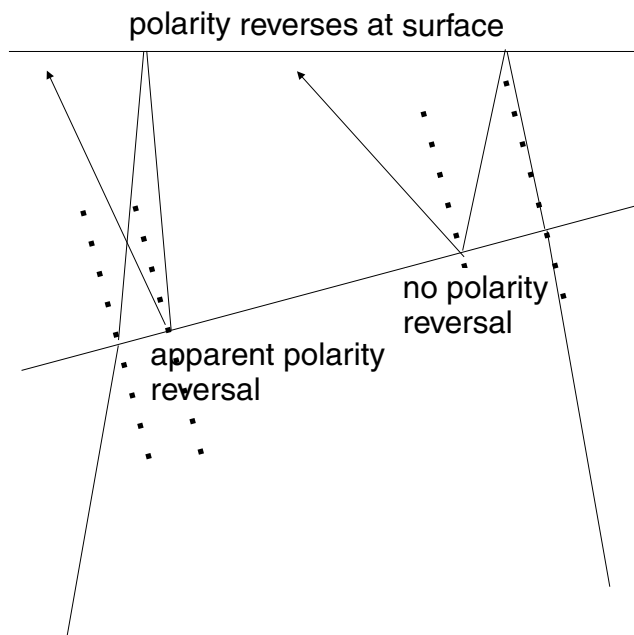
polarity reverses at surface

no polarity
reversal

apparent polarity
reversal

Figure 7. Schematic diagram explaining reversal of polarity of *PpP* phase for arrivals coming from opposite directions with respect to a dipping interface. The dashed line is perpendicular to the interface.

earlier than corresponding arrivals in the data, suggesting either that the modelled crust is too fast or the boundaries are too shallow.

We tested another model with a fast layer of 8.4 km s^{-1} *P* wave velocity at the top of the slab, after Gubbins & Snieder (1991). However, the synthetic seismograms produced were negligibly affected.

4.3.2 Anisotropic models: fit to SNZO

To try to model the polarity switch across backazimuths for the radial component arrival at 3 s, we turn to anisotropic models with dipping boundaries. We develop models to simulate the SNZO RFs. We show one model (TAR: Table 2) to compare to the Tararua array.

Model ANID20 (Table 2) combines features of the preferred models of sn116 (Savage 1998) and SNZO (Bourne & Stuart 2000). The top layers of sn116 are combined for the top 6.7 km. However, because the codes require the top layer to be isotropic, we use an isotropic top layer rather than the anisotropic surface layer in model sn116. An anisotropic layer in the lower crust is assumed, with 4 per cent anisotropy for both *P* and *S* and a horizontal slow axis of symmetry striking at 135° (updip of the slab), so the fast shear wave polarization is 45°. A low-velocity zone exists from 28 to 32 km depth, corresponding to the sediments at the top of the slab. The low-velocity zone is made slightly anisotropic (4 per cent for *P* and *S*), with a slow, vertical axis of symmetry since they are sedimentary layers. The oceanic crust has the same anisotropy symmetry system as the lower crust, but with higher anisotropy (6 per cent). The mantle has a fast, horizontal axis of symmetry based on *Pn* studies, with 7 per cent *P* and 5 per cent *S* anisotropy. The dip of model layers in ANID20 is 20°, compared to 15° for model ISO_NOLOW.

Much of the radial and transverse energy in the observed RFs is surprisingly well represented by RFs computed from ANID20 (compare Fig. 4 with Fig. 8), in both cases without multiples and with all multiples included. The features matched by the isotropic models are preserved. In addition, the anisotropy in the sedimentary layer at the top of the slab induces a reversal in the radial amplitudes

(3) at about 4 s for backazimuth 60°–180°, which is observed at 3 s for data but not at all for the isotropic models ISO_NOLOW or ISO_LOW.

Aspects of the Model ANID20 radial synthetics without multiples that do not fit the data include the larger amplitude on phase (2) at 1 s compared to the direct arrival (1) for backazimuth 260°–330° (compare Fig. 4 with Fig. 8). Similarly, the amplitude of the Moho arrival (4) at 5 s delay is larger on the synthetics than the data. In addition, the trough (3) associated with the low-velocity layer in the synthetics is placed at later times than the data. As discussed above for the isotropic model ISO_NOLOW, a more gradational layer structure would decrease the amplitude of the later arrivals, making them closer to the data. Some of the other problems are resolved by including interference with multiple reflections in the synthetic seismograms: negative polarity at 2.5 s from 60° to 180° backazimuth in the data is matched by that from the *PpP* phase in the top layer as discussed above. As discussed previously, observed multiples may be smaller than those predicted due to lateral inhomogeneity on interfaces. Therefore, we expect the response of the shallow Earth to lie somewhat between that of the synthetics with and without multiples, as observed.

The transverse arrivals of the synthetics match the data in character, in that the largest arrivals occur for backazimuth 200°–260° in both. The general character at these backazimuths between 0 and 6 s is also fit fairly well, with a peak just preceding a trough at 5–6 s, and a positive initial pulse (Fig. 8). The amplitudes with the anisotropic model are higher than those with the isotropic model ISO_NOLOW (Fig. 4), and the data is in between. However, the rest of the backazimuths do not match as well. The polarity of the initial transverse pulses at most backazimuths are similar in the data and synthetics, but they arrive just after the 0 s delay in the data, while they arrive at exactly 0 s with the synthetics.

4.3.3 Model parameter sensitivity: effect on midcrustal positive arrival (2)

We examine the sensitivity of the model to various parameters by calculating synthetics based on similar models. We first vary features of layer dip, anisotropy and plunge of axis of symmetry to determine qualitative effects on the arrivals. Later we try to fit the timing of arrivals by changing depths of interfaces.

Layer Dip: we begin by discussing the effect of different models on the midcrusal positive arrival (2). Model ANI2FLATD20 resembles ANID20 except that the top interface at 6.7 km is flat rather than dipping (Table 2, Fig. 8). The amplitudes of phase (2) at 1.5 s are smaller than those with a dipping layer, because less energy is deflected away from the initial vertical *P* wave; it is now smaller than the initial *P* wave, closer to the data, and the transverse energy in the initial *P* wave is much smaller. However, the width of the initial radial *P* wave is less dependent on backazimuth, and so fits less well to the data. It seems likely that the real dip of the layer lies between this flat model and the slab dip. Model ANID15 resembles ANID20 except interface dips are 15° (Table 2). This dip agrees with the delay time moveout of the Moho *Ps* across the Tararua array (see Section 3 above), and was also suggested by other studies near SNZO (e.g. Davey & Smith 1983), though not the most recent (Reading *et al.* 2001). The arrival at 1.5 s is smaller with the smaller dip, and this is closer to the data. However, as discussed above, the interface is deeper and yet flat under the Tararua array to the northeast. A test with a dip to the northeast (not shown) did not exhibit the width changes of the initial *P* wave at the correct backazimuth,
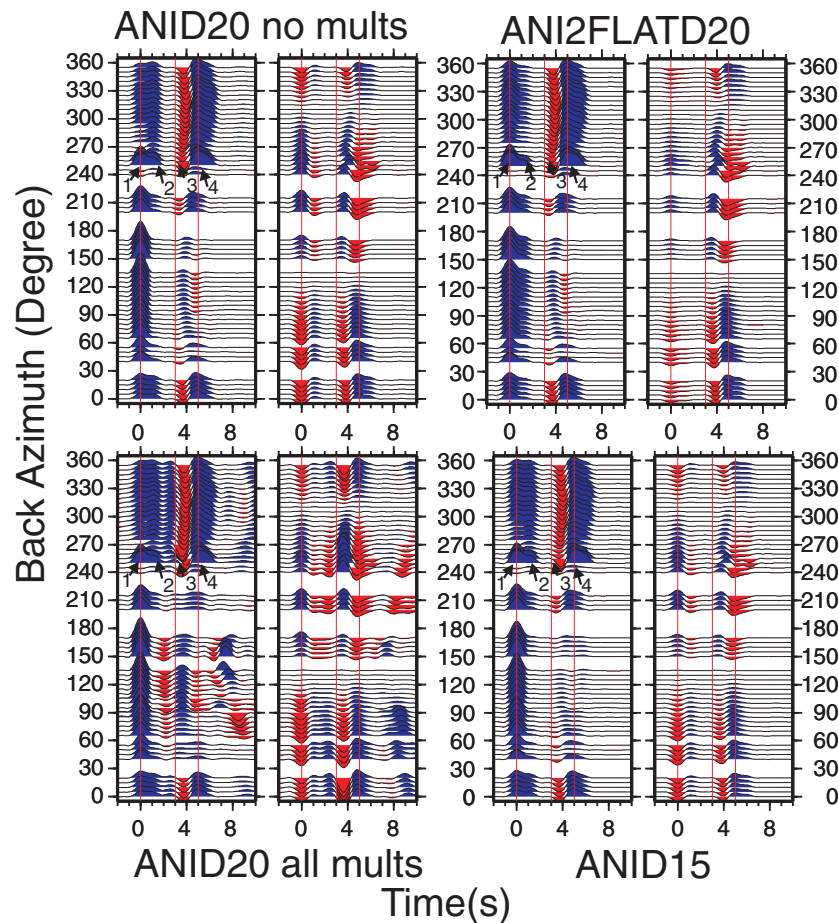
Figure 8. Comparison of anisotropic models ANID20, ANID15, and ANI2FLATD20 (Table 2), as in Figs 3–6. Scale is the same used in Fig. 4.

so we suggest the strike of the dipping layer under SNZO is close to the slab strike.

Anisotropy effect: model ANI2ANID15 resembles model ANID15 (Table 2), except for a shallow anisotropic layer after Savage (1998). The slow axis of symmetry in the second layer has 45° strike, so that the fast polarization lies at 135°, consistent with the shallow upper layer anisotropy measured at station KSE, which was nearly collocated with SNZO (Gledhill 1993). There is little difference between synthetic seismograms for models ANI2ANID15 and ANID15, so we do not show a plot, and the lack of variation can be seen in the initial pulses being consistent for models discussed below and ANID15. (compare Fig. 9 to Fig. 8).

4.3.4 Effect on slab arrivals (3) and (4)

The synthetic seismograms for model ANID15 are similar to those from model ANID20, but the peak at 5 s and the trough before it, as well as the reversal of these phases from 60°–180° backazimuth, are less pronounced using model ANID15 with the smaller interface dip (Fig. 8).

Effect of symmetry axis plunge: the amplitudes of the arrivals at 3–5 s can be increased by adding a plunge of +5° to all the anisotropic symmetry axes in the dipping layers (compare model ANI2ANIP5D15 to model ANID15, Table 2, Figs 8–9), but the amplitudes are still smaller than with a dip of 20° (Model ANID20, Fig. 8). Therefore, there is a tradeoff between dip of the inter-

faces and plunge of the axes of symmetry. Allowing the symmetry axis of the lower crust to be vertical instead of horizontal (ANI2ANIP90D20; Table 2; Fig. 9) removes the positive arrivals (3) at 3.5 s for 90°–180° backazimuth, thus representing the data less well than the other models. Model ANI2ANI3ISOD20 resembles ANI2ANIP90D20 and ANID20, but with isotropic lower crust. The arrivals are nearly indistinguishable from those of model ANID20.

One might expect that the metasediments on top of the slab would be tilted with the slab, so that the axis of symmetry would plunge at 70° for the 20° dipping slab, instead of vertically. When we tried this with a horizontal axis of symmetry in the crust (not shown) we again removed the peaks (3) at 3.5 s for 90°–180° backazimuth. Next we included both the plunge of 70° in the metasediment layer and an axis of symmetry in the crust plunging at 30°, as suggested by Brisbourne *et al.* (1999) on the basis of observations of anomalous surface wave polarities. In this case, the crustal plunging axis of symmetry produced the correct polarity of *Ps* arrival (3) (ANIP30D20, Fig. 9). Examining varying plunges of the axis of symmetry in the crust suggests that the most important factor in matching the positive arrival at 3 s for the 90°–180° backazimuth range is the change in plunge of the axis of symmetry from vertical in the low-velocity region at the top of the slab to horizontal, or isotropic, in the layer above, or else from slab-perpendicular in the low-velocity region to crustal plunges between 20° and 50°.

Several aspects of the receiver functions are not fit with the models presented above, including the timing of phases (3) and (4). In addition, the amplitude of the beginning of (4), which is caused by
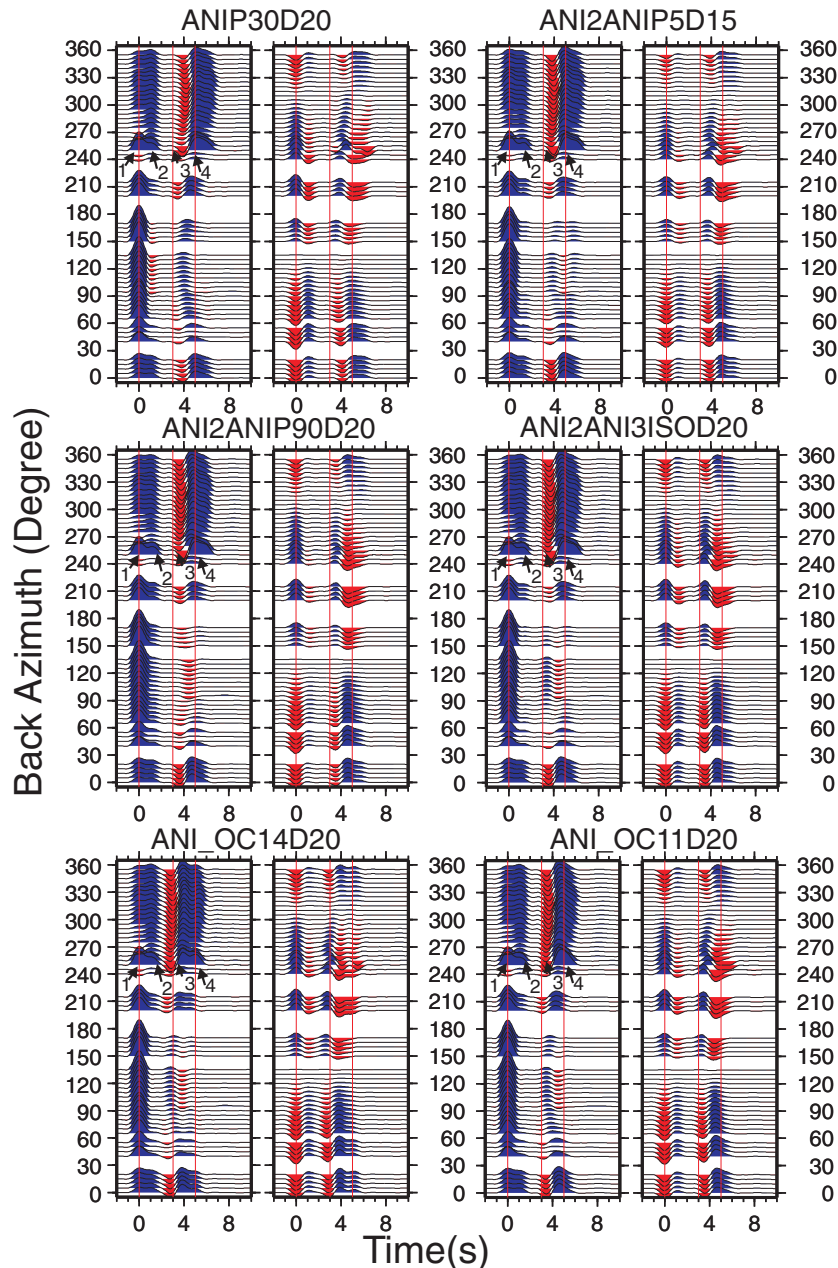
Figure 9. Comparison of anisotropic models (Table 2) as in Figs 3–7.

the transition from the low-velocity layer at the top of the slab to the crustal velocities of the slab, is too high in the models (it is nearly absent in the data; Figs 3, 4 and 8). This suggests that the transition across this boundary is more gradational than the model. A plethora of multiples make it computationally taxing to model a gradational boundary with the Frederiksen & Bostock (2000) seismogram code. Instead, to fit the timing better, we combine models ANID20 and ISO_LOW and adjust the thickness of the lower crust in the Australian plate, and the Moho in the oceanic plate, to change the timing of the trough and the end of the Moho peak on the radial component, respectively. High-frequency RFs suggest that the end of the later part of the 'Moho peak' is caused by the transition from oceanic crust to mantle. Models ANI_OC14D20 and ANIOC11D20 are end members (Figs 9, 10; Table 2). The thickness of the low-velocity layer (LVL) is set to 4 km in both models. If we prescribe a narrower

thickness of 2 km, as suggested by the *ScS–P* conversion modelling (Bourne & Stuart 2000), a narrower and smaller amplitude trough results, which fits the data less well. Model ANI_OC14D20 has the top of the LVL at 21 km, as given by Reading *et al.* (2001), and the oceanic Moho at 35 km, for an oceanic crustal thickness of 14 km. Model ANIOC11D20 has an 11 km oceanic crust, with the top of the LVL at 26 km and the oceanic Moho at 37 km. Model ANI_OC14D20 matches better the timing of the positive polarity *Ps* (3) from the LVL at 60°–180° backazimuth, while model AN-IOC11D20 matches better the timing of the negative polarity *Ps* (3) for 210°–330° backazimuth (compare models in Fig. 9 with data in Fig. 4). Model ANIOC11D20 also provides a better match to the timing of the largest Moho *Ps* peak, and the timing and amplitudes of the large transverse *Ps* between 3 and 6 s for 180°–270° backazimuth. We therefore prefer model ANIOC11D20.
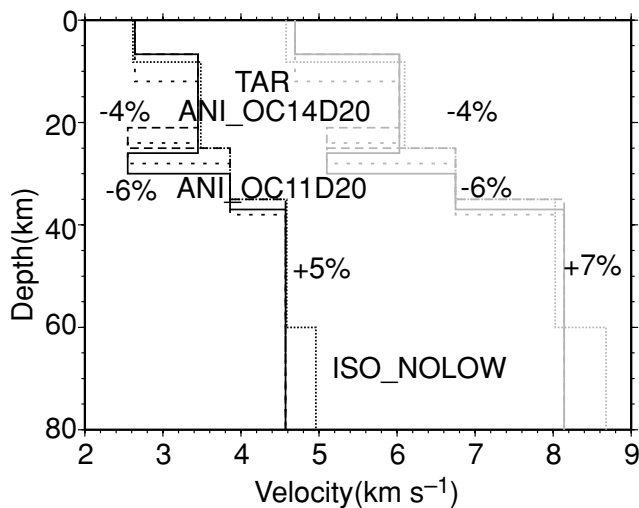
Figure 10. Sample velocity models detailed more explicitly in Table 2. *P* and *S* velocities are grey and black, respectively. Numerals represent the per cent anisotropy, which is common to each model. Solid line: model ANIOC11D20 (our preferred model). Long dashes: model ANI_OC14D20. Short dashes: model TAR. Dotted line: model ISO_NOLOW. All models dip with the slab (Table 2).

4.3.5 Model TAR: fit to Tararua array

We present one model, TAR, for the Tararua array to compare it to the data for the western arm (Table 2; Figs 10–11). The shallowest interface is flat and has a depth of 12 km, to be consistent with its arrival at every station at 2 s as discussed above. We adapt the layers above and within the slab from model ANIOC11D20. We decrease slab dip to 12.6°, reflecting the shallower dip measured under the Tararua array (Reading *et al.* 2001). The depth to the top of the slab interface is set to 24 km beneath station W1 (Fig. 1; Reading *et al.* 2001). We modified other interface depths to match the timing of the major arrivals. The timing and average relative amplitudes of the 2-s pulse of the radial synthetics match well to the data (compare Fig. 11 with Figs 5 and 6). As previously noted for station SNZO, the synthetics predict higher amplitudes for the slab-converted *Ps* phases than estimated from data, suggesting that the transition may be more gradational at this period range, compared to the period of the *ScS* waves used to determine the velocity contrasts (Bourne & Stuart 2000). There is also less of a difference for the two backazimuth ranges considered in the synthetics than that in the data, and the transverse arrivals are more coherent across the synthetics than across the data.

4.3.6 Non-uniqueness

Seismic velocities trade off with interface depths in models that would fit the observed RFs. For example, a 1 km s^{-1} change in velocity would be compensated by a 0.5-km change in the LVL thickness, because we estimate our ability to match the timing to ±0.5 s. Our two estimates for the thickness of the oceanic crust, of 14 and 11 km, are closer to the 13 km reported by (Bourne & Stuart 2000) for SNZO than to 16 ± 2 km suggested by (Reading *et al.* 2001) on the basis of the thickness of a 'double band' of seismicity in the region. Further attempts at modelling could be carried out to match the remaining features that are not perfectly matched with the synthetics. However, differences between synthetic RFs with all

Ps multiples and those without any multiples suggests that detailed modelling might be premature until we can estimate better how much of the multiple energy should be kept.

Moveout with epicentral distance is also similar for the synthetics and the data (Fig. 12), although we could not get stable results for the synthetics for the smallest epicentral distances.

4.4 Comparison to Savage (1998) paper and interpretation of the anisotropic layer above the slab

Earlier forward modelling of a much smaller SNZO data set suggested that anisotropy was more important than dipping layers to explain the changes in the radial and transverse arrivals (Savage 1998) between 4 and 6 s. The change in polarity of the radial amplitude at 3 s had not been apparent with the smaller SNZO data set. To achieve observed RF amplitudes on the transverse and radial components with flat boundaries required both a plunge of the axis of symmetry and a high anisotropy (12 per cent) within the subducted oceanic crust. We note here that a mistake in the earlier paper led to the plunge being reported with the wrong sign. The correct description of the plunge used in the synthetics in that paper was for the (slow) symmetry axis to be plunging at 20°–40° from horizontal, down to the northwest. For simplicity the plunge of the axis of symmetry in this layer has been considered horizontal in the models presented here. The amount of anisotropy required in the oceanic crust to fit the arrival amplitudes decreases when dipping boundaries and anisotropy are combined. Thus, the 6 per cent anisotropy used in the synthetics here is sufficient to achieve the observed amplitudes of the trough in the transverse arrivals at 5 s from backazimuth 200° to 270° (compare Fig. 9 with Figs 4 and 8). Park *et al.* (2004) noted also that the effect of slab dip lowered the strength of anisotropy needed to fit *Ps* converted waves from the Cascadia slab beneath GSN Station COR (Corvallis, Oregon).

Anisotropy with a vertical or slab-perpendicular axis of symmetry in the LVL is not surprising. Sedimentary layers have a vertical axis of symmetry, and subducted sediments at a depth of 20 km should be metamorphosed. We estimate the rock types in the following manner. Low heat flow of 21–29 mW m^{-2} was determined in southern North Island (Pandey *et al.* 1991), and high *Vp* imaged in the slab to the north also suggests a cool slab (Reyners *et al.* 2005). Cool subduction zones lie within the blueschist facies at the shallow depths in this study, and the clay minerals in the sediments should form mica (e.g. Peacock 2003). Micas are highly anisotropic minerals, and are expected to have near-vertical symmetry axes under these conditions (e.g. Babuska & Cara 1991).

Using high-frequency local earthquakes, Reading *et al.* (2001) found stronger *Ps* and *Sp* conversions from the slab interface at points located to the northeast than they do near the stations we have examined. They suggested that the lack of such strong conversions at the Tararua array and SNZO means that thick layers of sediments are confined to the northeastern region. Yet a trial model (not shown) without a low-velocity layer at the top of the slab was unable to produce the correct polarity of the phase '3' in Fig. 3. Thus our results and the *ScSP* conversions reported in Bourne & Stuart (2000) suggest that subducted sediments extend beneath the Tararua array. We suggest that the contrast in rock properties may occur over a thicker depth range near the stations in this study, so that the lower frequencies of teleseismic earthquakes are affected, while the higher-frequency, local earthquake signals transmit through gradational elastic contrasts without sharp isolated *Ps*-converted phases.
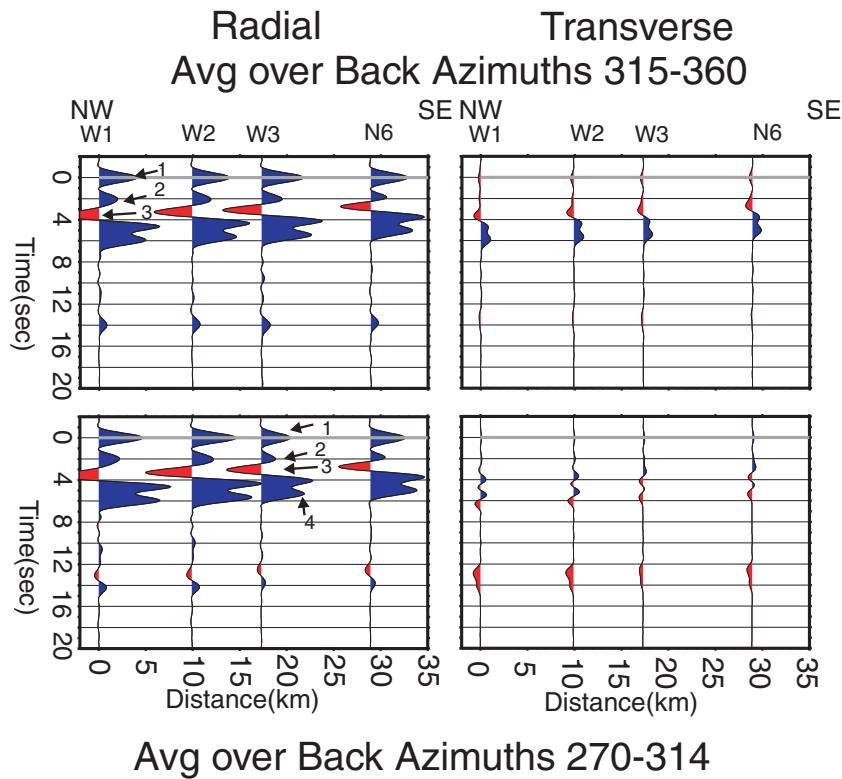
Figure 11. Synthetic seismogram calculated for western Tararua stations for model TAR, plotted as in Fig. 5 and 6. Left: Radial Right: Transverse Top: Stack over back azimuth 315°–360°. Bottom; Stack over back azimuth 270°–315°.

5 SUMMARY

Strong backazimuthal variations of both the radial and transverse receiver functions observed previously at station SNZO (Savage 1998) have been confirmed by an enhanced data set from more stations, for a longer time period and from a more sophisticated calculation of the receiver functions.

A qualitative fit to the azimuthal variation of the data at SNZO has been achieved by including dipping boundaries separating anisotropic material, both within and above the subducting oceanic slab. The dipping boundaries allow the amplitude variations on the transverse and radial components to be fit with smaller anisotropy (4–6 per cent) than was needed in the modelling of the flat anisotropic layers (12 per cent) by Savage (1998).

The observed RFs have smaller amplitudes than those calculated from layer velocities previously determined from *ScSP* phases (Bourne & Stuart 2000). The amplitudes of the multiple reflections are also smaller in the data than the models. This suggests three possibilities, perhaps in combination. (1) The change in velocity may be more gradational at these periods than at the longer periods in the *ScSP* study; (2) there may be strong attenuation in the near surface; and (3) interfaces may be rough, so that reflected energy is scattered incoherently.

A reversal in polarity for the radial component at 3 s at SNZO, between backazimuth 200°–360° compared to 90°–180° can be explained by a low-velocity layer at the top of the subducting oceanic crust that has a vertical slow axis of symmetry The plunge of this symmetry axis is constrained by the presence or absence of a *Ps* polarity reversal and depends also on the plunge of the axis of symmetry in the layer above it. A plunge normal to the slab can produce the polarity reversal if the crustal symmetry axis plunges at 30°, as

expected for crack-controlled anisotropy parallel to dips of nearby faults. There is a tradeoff between the plunge and the anisotropy needed to fit the *Ps* amplitudes. Sediments metamorphosed in the blueschist facies are likely candidates for the low-velocity layer. Reversals in phase can also occur for *PpP* multiples in isotropic dipping layers, but cannot explain this phase at 3 s.

The thickness of the schist layer is not well constrained; to fit the breadth of the pulse it is modelled as 4 km thick, which also allows modest anisotropy. If the layer is thinner, then stronger anisotropy will be needed to achieve the amplitudes visible in the data.

The Tararua array, which only has dense data coverage for backazimuth 280°–340°, confirms the arrival at 5 s from the Moho within the slab. Its transverse arrivals are less prominent than those at SNZO, confirming the shallower dip of the plate interface in the model of Reading *et al.* (2001). The transverse arrivals differ between the western arm and the northern arm of the Tararua array. The 'slab-converted' *Ps* arrives earlier on stations that are above shallower sections of the subducting plate, and the arrivals suggest the slab is dipping about 15° beneath the array.

The Tararua array records a strong, consistent *Ps* phase at 2 s delay relative to direct *P*. The phase may correspond to an arrival occurring at 1.5 s at SNZO, which suggests that the layer shallows to the south. We interpret the phase as converted from the boundary between a lower velocity layer above to a higher velocity layer at about 12 km depth under the Tararua array, and 7 km under SNZO. The upper layer is interpreted as greywacke of the Torlesse Terrane, and the lower layer may correspond to the more schistose Waipapa Terrane. However, if the lower crust is schistose, then as discussed in point 4 above, its anisotropy is either small or has non-horizontal schistocity at the interface between it and the oceanic sediments. A
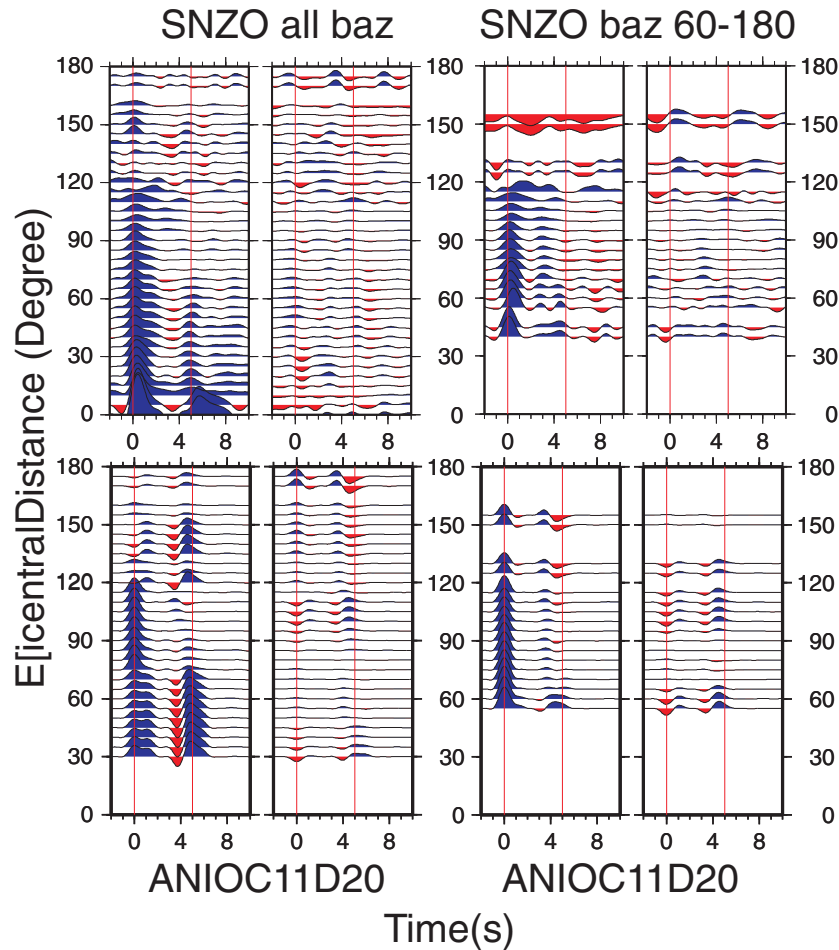
Figure 12. Comparison of RFs plotted as a function of epicentral distance for data at SNZO and synthetics from model ANIOC11D20 (Table 2). Layout as in Fig. 3 except that the vertical axis is epicentral distance here. The scale is the same as that in Fig. 3. Top panel: SNZO data. Bottom panel: synthetic seismograms from model ANIOC11D20. Left-hand panel: all backazimuths stacked (represented most heavily by backazimuth 270–360). Right-hand panel: stacked for backazimuth 60°–80°.

near- horizontal orientation of the axis of symmetry, that is, near-vertical layering, is also consistent with shear wave splitting in the crust (Gledhill 1991), with the previous interpretation at SNZO (Savage 1998), and with interpretations of receiver functions in the northern South Island (Wilson *et al.* 2004). It is likely caused by shear from present and previous strike-slip deformation.

A holistic modelling approach to constrain tradeoffs between anisotropic strength, layer thicknesses and plunges of the axes of symmetry, is recommended for complex structures above subduction zones. This modelling should include a methodology for including multiple arrivals as smaller than expected purely from velocity changes without attenuation.

ACKNOWLEDGMENTS

REFERENCES

Aki, K. & Richards, P.G., 1980. *Quantitative Seismology, Theory and Methods,* W.H. Freeman and Company, San Francisco.

Ammon, C.J., Randall, G.E. & Zandt, G., 1990. On the non-uniqueness of receiver function inversions, *J. geophys. Res.,* **95,** 15 303–15 318.

Anderson, H. & Webb, T., 1994. New Zealand seismicity: patterns revealed by the upgraded National Seismograph Network, *N. Z. J. Geology and Geophys.,* **37,** 477–493.

Babuska, V. & Cara, M., 1991. *Seismic Anisotropy in the Earth,* Kluwer Academic Publishers, Dordrecht/Boston/London.

Bannister, S., 1988. Microseismicity and velocity structure in the Hawkes Bay region, New Zealand, *Geophys. J.,* **95,** 45–62.

Bourne, M. & Stuart, G., 2000. ScSp observed on North Island, New Zealand; implications for subducting plate structure, *Geophys. J. Int.,* **142**(3), 925–932.

Brisbourne, A.G. & Stuart, G.W., 1998. Shear-wave velocity structure beneath North Island, New Zealand, from Rayleigh-wave interstation phase velocities, *Geophys. J. Int.,* **133,** 175–184.

Brisbourne, A.G., Stuart, M. & Kendall, J.M., 1999. Anisotropic structure of the Hikurangi subduction zone, New Zealand–integrated interpretation of surface-wave and body-wave observations, *Geophys. J. Int.,* **137,** 214–230.

Cassidy, J.F., 1992. Numerical experiments in broadband receiver function analysis, *Bulletin - Seismological Society of America,* **82**(3), 1453–1474.

Chadwick, M., 1997. Hikurangi margin seismic experiment, *PhD Thesis,* Victoria University of Wellington, Wellington.

Darby, D.J. & Beanland, S., 1992. Possible source models for the 1855 Wairarapa earthquake, New Zealand, *J. geophys. Res.,* **97**(B9), 12 375–12 389.

Davey, F.J. & Smith, E.G.C., 1983. A crustal seismic reflection-refraction experiment across the subducted Pacific plate under Wellington, New Zealand, *Phys. Earth planet. Inter.,* **31,** 327–333.

Eberhart-Phillips, D. & Reyners, M., 1997. Continental subduction and three-dimesional crustal structure: the northern South Island, New Zealand., *J. geophys. Res.,* **102**(B6), 11 843–11 861.

Eberhart-Phillips, D. & Reyners, M., 1999. Plate interface properties in the northeast Hikurangi subduction zone, New Zealand, from converted seismic waves, *Geophys. Res. Lett.,* **26**(16), 2565–2568.

Eiler, J., 2003. *Inside the Subduction Factory,* 311 p., American Geophysical Union, Washington, DC.

Ferris, A., Abers, G.A., Christensen, D.H. & Veenstra, E., 2003. High resolution image of the subducted Pacific (?) plate beneath central Alaska, 50–150 km depth, *Earth planet. Sci. Lett.,* **214**(3–4), 575–588.

Frederiksen, A.W. & Bostock, M.G., 2000. Modelling teleseismic waves in dipping anisotropic structures, *Geophys. J. Int.,* **141**(2), 401–412.

Frederiksen, A.W., Folsom, H. & Zandt, G., 2003. Neighbourhood inversion of teleseismic Ps conversions for anisotropy and layer dip, *Geophys. J. Int.,* **155**(1), 200–212.

Galea, P., 1992. Observations of very high P-velocities in the subducted slab, New Zealand, and their relation with the slab geometry, *Geophys. J. Int.,* **110,** 238–250.

Garrick, R.A., 1968. A reinterpretation of the Wellington crustal refraction profile, *N. Z. J. Geology and Geophys.,* **11,** 1280–1294.

Gledhill, K.R., 1991. Evidence for shallow and pervasive seismic anisotropy in the Wellington region, New Zealand, *J. geophys. Res.,* **96,** 21 503–21 516.

Gledhill, K.R., 1993. Shear waves recorded on close-spaced Seismographs: II. The complex anisotropic structure of the Wellington Peninsula, New Zealand, *Can. J. Expl. Geophys.,* **29**(1), 299–314.

Gubbins, D. & Snieder, R., 1991. Dispersion of P waves in subducted lithosphere: Evidence for an eclogite layer, *J. geophys. Res.,* **96,** 6321–6333.

Ingham, M., Whaler, K. & McKnight, D., 2001. Magnetotelluric sounding of the Hikurangi Margin, New Zealand, *Geophys. J. Int.,* **144**(2), 343–355.

Kennett, B.L.N., Engdahl, E.R. & Buland, R., 1995. Constraints on seismic velocities in the Earth from traveltimes, *Geophys. J. Int.,* **122**(1), 108–124.

Kreemer, C., Holt, W.E. & Haines, A.J., 2003. An integrated global model of present-day plate motions and plate boundary deformation, *Geophys. J. Int.,* **154,** 8–34.

Langston, C.A., 1977. Corvallis, Oregon, crustal and upper mantle receiver structure from teleseismic *P* and *S* waves, *Bull. seism. Soc. Am.,* **67,** 713–724.

Levin, V. & Park, J., 1997. P-SH conversions in a flat-layered medium with anisotropy of arbitary orientation, *Geophys. J. Int.,* **131**(2), 253–266.

Levin, V. & Park, J., 1998. P-SH conversions in layered media with hexagonally symmetric anisotropy: a cookbook, *Pure appl. Geophys.,* **151**(2–4), 669–697.

Louie, J.N., Chavez-Perez, S., Henrys, S. & Bannister, S., 2002. Multimode migration of scattered and converted waves for the structure of the Hikurangi slab interface, New Zealand, in *Deep seismic probing of the continents and their margins,* pp. 227–246, ed. Thybo, H., Tectonophysics.

Lucente, F.P., Piana Agostinetti, N., Moro, M., Selvaggi, G. & Di Bona, M., 2005. Possible fault plane in a seismic gap area of the southern Apennines (Italy) revealed by receiver function analysis, *J. geophys. Res.,* **110,** B04307, doi:10.1029/2004JB003187.

Luo, X., 1992. Subduction interface and crustal structure in the Cape Palliser region, North Island, New Zealand, from observations of Cape Palliser earthqaukes, *N. Z. J. Geology and Geophys.,* **35**(4), 491–499.

Mortimer, N., Tulloch, A.J. & Ireland, T.R., 1997. Basement geology of Taranaki and Wanganui Basins, New Zealand, *N. Z. J. Geology and Geophys.,* **40,** 223–236.

Owens, T.J., Zandt, G. & Taylor, S.R., 1984. Seismic evidence for an ancient rift beneath the Cumberland Plateau, Tennessee, *J. geophys. Res.,* **89,** 7783–7795.

Özalaybey, S., Savage, M.K., Sheehan, A.F., Louie, J.N. & Brune, J.N., 1997. Shear-wave velocity structure in the northern Basin and Range province from the combined analysis of receiver functions and surface waves, *Bull. seism. Soc. Am.,* **87,** 183–199.

Pandey, O.P., Cermak, V. & Rybach, L., 1991. Terrestrial heat flow and lithospheric geothermal structure in New Zealand, in *Terresterial heat flow and the lithosphere structure,* pp. 338–380, Springer Berlin [u.a.]

Park, J. & Levin, V., 2000. Receiver functions from multiple-taper spectral correlation estimates, *Bull. seism. Soc. Am.,* **90**(6), 1507–1520.

Park, J. & Levin, V., 2002. Geophysics: Seismic anisotropy: Tracing plate dynamics in the mantle, *Science,* **296**(5567), 485–489.

Park, J. & Levin, V., 2006. Receiver functions from multiple-taper spectral correlation: Statistics, single-station migration, and jackknife uncertainty, *Geophys. J. Int.,* submitted.

Park, J., Levin, V., Brandon, M., Lees, J.M., Peyton, V., Gordeev, E. & Ozerov, A., 2002. A dangling slab, amplified arc volcanism, mantle flow and seismic anisotropy in the Kamchatka Plate corner, *Geodynamics Series,* **30,** 295–324.

Park, J., Yuan, H.Y. & Levin, V., 2004. Subduction zone anisotropy beneath Corvallis, Oregon: A serpentinite skid mark of trench-parallel terrane migration?, *Journal of Geophysical Research-Solid Earth,* **109**(B10), doi:B10.1029/2003JB002718.

Peacock, S.M., 2003. Thermal structure and metamorphic evolution of subducting slabs, in *Inside the Subduction Factory,* pp. 7–22, ed. Eiler, J., American Geophysical Union, Washington, DC.

Reading, A., 1996. Deep lithospheric structure from multi-phase seismic tomography: the subduction zone beneath southern North Island, New Zealand, *Type thesis Thesis,* University of Leeds, Leeds.

Reading, A.M., Gubbins, D. & Mao, W.J., 2001. A multiphase seismic investigation of the shallow subduction zone, southern North Island, New Zealand, *Geophys. J. Int.,* **147**(1), 215–226.

Reyners, M., Eberhart-Phillips, D., Stuart, G. & Nishimura, Y., 2005. Imaging subduction from the trench to 300 km depth beneath the central North Island, New Zealand, with Vp and Vp/Vs, *Geophys. J. Int.,* **165,** 565–583.

Robinson, R., 1986. Seismicity, structure and tectonics of the Wellington region, New Zealand, *Geophys. J. R. astr. Soc,* **87,** 379–409.

Savage, M.K., 1998. Lower Crustal anisotropy or dipping boundary? Effects on receiver functions and a case study in New Zealand, *J. geophys. Res.,* **103**(7), 15 069–15 089.

Shafkit, A., 1997. A Receiver Function Study of the Hikurangi Subduction Zone, NZ, *PhD Thesis,* University of Leeds, Leeds.

Stewart, D., 1998. Earth velocity structure from an earthquake recording array, *Honours Thesis,* Victoria University of Wellington, Wellinton.

Stuart, G., Francis, D., Gubbins, D. & Smith, G., 1995. Tararua broadband array, North Island, New Zealand, *Bull. seism. Soc. Am.,* **85**(1), 325–333.

Tatsumi, Y. & Kogiso, T., 2003. The subduction factory; its role in the evolution of the Earth's crust and mantle, in *Intra-oceanic subduction systems; tectonic and magmatic processes,* pp. 55–80, eds Larter, R.D. & Leat, P.T., Geological Society, United Kingdom.

Todd, H., 2002. An investigation of upper mantle structure beneath the Tararua Ranges, North Island, New Zealand using receiver functions, *Honours Thesis,* Victoria University of Wellington, Wellington.

Walcott, R.I., 1987. Geodetic strain and the deformational history of the North Island of New Zealand during the late Cainozoic, *Phil. Trans. R. Soc. Lond.,* A., **321,** 163–181.

Wessel, P. & Smith, W.H.F., 1998. New, improved version of the Generic Mapping Tool released, *EOS, Trans. Am. geophys. Un.,* **79,** 579.

Wilson, C.K., Jones, C.H., Molnar, P., Sheehan, A.F. & Boyd, O.S., 2004. Distributed deformation in the lower crust and upper mantle beneath a continental strike-slip fault zone; Marlborough fault system, South Island, New Zealand, *Geology,* **32**(10), 837–840.

Yuan, X. et al., 2000. Subduction and collision processes in the Central Andes constrained by converted seismic phases, *Nature,* **408,** 958–961.